Received: 9 March 2018 | Revised: 22 June 2018 | Accepted: 23 June 2018

DOI: 10.1002/nag.2845

RESEARCH ARTICLE

WILEY

Multiaxial cyclic plasticity in accordance with 1D hyperbolic models and Masing criteria

Doriam Restrepo[1] | Ricardo Taborda[2,3]

[1]Departamento de Ingeniería Civil, Universidad EAFIT, Medellín, Colombia

[2]Department of Civil Engineering and Center for Earthquake Research and Information, The University of Memphis, Memphis, Tennessee

[3]Escuela de Ingeniería, Universidad EAFIT, Medellín, Colombia

Correspondence
Doriam Restrepo, Departamento de Ingeniería Civil, Universidad EAFIT, Medellín, Colombia.
Email: drestre6@eafit.edu.co

Funding information
Universidad EAFIT; US National Science Foundation (NSF), Grant/Award Number: ACI-1450451

Summary

Bounding surface plasticity models based on one-dimensional hardening functions are broadly accepted as a valid approach to represent the multiaxial cyclic behavior of undrained cohesive soils. However, under certain conditions, these models may exhibit deviations from the expected stress path. This makes them inadequate to meet traditional hysteretic rules. Current solutions to this problem impose thresholds to help adjust the stress path by introducing additional memory variables. This article presents a formulation that achieves the same goal without the need of such additional variables. The proposed formulation operates on a generic hardening function under multiaxial loading while preserving the simplicity inherited from pure deviatoric bounding surface models. In addition, the approach presented here allows the implementation of Masing-type rules, as well as the use of reduction factors to mitigate the overdamping effects of large hysteresis loops. The formulation is tested using well-known hyperbolic backbone functions under radial and nonradial multiaxial loading cycles, and it is shown to have good agreement with reference solutions.

KEYWORDS

bounding surface, hyperbolic models, multiaxial response, soil nonlinearity

1 | INTRODUCTION

There exist a variety of one-dimensional nonlinear soil constitutive models based on the concept of backbone curves (eg, previous studies[1-4]) and Masing-type rules[5] to control the evolution of the stress-strain relationship during nonlinear excursions under cyclic loading conditions. These models are broadly used in different engineering applications, from earth structures to seismic site response.

One-dimensional nonlinear soil models are often preferred because they are better than other approximate approaches such as the linear equivalent method[6,7] and because—in most cases—their parameters can be easily related to laboratory test (eg, shear moduli degradation curves and evolution of damping with level of deformation). However, it is well known that three-dimensional effects due to geometric or input motion complexities play a significant role in the mechanical performance of geomaterials (eg, Xu et al[8] and Taborda et al[9]). Therefore, adequate models that can simulate nonlinear soil behavior under multiaxial, arbitrary (cyclic) loading conditions are necessary.

From a geomechanical perspective, this problem has been most successfully addressed using models based on the theories of bounding surface plasticity (eg, Dafalias and Popov[10,11]) and multiyield surface plasticity (eg, Prévost[12,13]). These methods offer robust frameworks for representing the multiaxial mechanical behavior of geomaterials, but from a

practical perspective, the constitutive models arising from them often pose computational disadvantages. They tend to be more difficult to implement, have large numbers of parameters, and be calibrated for specific applications (eg, Kramer [14]).

Alternatively, the formulation proposed by Borja and Amies[15] provides a link between the theory of bounding surface plasticity and the one-dimensional method. Initially formulated for the case of undrained cohesive soils, Borja and Amies[15] adopt a von Mises bounding surface fixed in the stress space and consider a material with a vanishing elastic region. As a result, hardening depends only on the distance from the current stress point to its image point on the bounding surface and the last stress-strain reversal. This reduces the integration of the constitutive model to solving two nonlinear equations (as opposed to the solution of nonlinear tensorial equations in more sophisticated models) and allows one to adopt a hardening function compatible with typical modulus reduction curves from one-dimensional formulations.

The methodology introduced by Borja and Amies[15] has since then been used in different types of problems in site response and soil-structure interaction (eg, previous studies[16-18]), and its ideas have been extended to other soil types (eg, Pisano and Jeremic[19]). Its success notwithstanding, there are shortcomings known to the methodology. In particular, setting the bounding surface fixed in the stress space causes the hysteresis loops not to close upon reaching the point of reversal after complete cycles.[20] Likewise, if unloading from the virgin curve occurs at a particular strain reversal, the absolute value of the unloading stress associated with the opposite strain reversal is always smaller than the reverse stress at loading. The same problem occurs—but more pronouncedly—in the form of overshooting generated by partial unloading-reloading cycles. As a result, the method does not comply with the first and extended Masing rules.

Montáns[20] offered a solution by artificially shifting the bounding surface to a virtual position determined by the last stress reversal. This approach modifies the original formulation and increases the complexity of the numerical integration. Others implemented fixes by adding thresholds to either the minimum distance between the current stress and the image stress (eg, Fardis et al[21] and Voyiadjis and Abu-Lebdeh[22]) or the accumulated plastic strain (eg, Dafalias[23] and Mojtaba and Taiebat[24]). While these solutions adequately address the aforementioned problems, the thresholds are nonunique, and their implementation requires the use of additional (arbitrary) memory variables. More recently, Numanoglu et al[25] presented a generalized model for cyclic loading, but the reported results were based on a parallel-series distributed element model.

This article presents a formulation that solves the same problems without the need of additional (artificial or user-defined) memory variables beyond those naturally required to recover the previous stress-strain reference conditions. The proposed formulation operates on the hardening function and introduces new functions for the unloading branches while preserving the simplicity inherited from the original framework (ie, Borja and Amies[15]). The proposed formulation works well under multiaxial loading and allows the implementation of Masing-type rules, as well as the use of the reduction factors proposed by Darendeli[26] and Phillips and Hashash[27] to mitigate the overdamping effects of large hysteresis loops. The formulation is tested using the Konder-Zelasko or KZ,[2] the modified Konder-Zelasko or MKZ,[3] and the GQ/H[4] hyperbolic hardening functions under radial and nonradial multiaxial loading cycles, and it is shown to have good agreement with provided reference solutions.

2 | MATERIAL UPDATE

Consider a J_2 material of vanishing elastic region, associative flow rule, and Prager's translation rule for the back-stress tensor, for which its rate magnitude is defined as

$$\|\dot{\boldsymbol{\alpha}}\| = 2/3H'\lambda, \tag{1}$$

where H' is the hardening function and λ is the plastic consistency parameter. Given such a material, Borja and Amies[15] showed that the deviatoric stress $\boldsymbol{s}$ and the deviatoric strain $\boldsymbol{e}$ tensors observe the relationship

$$\dot{\boldsymbol{s}} + \left(\frac{3G_{\max}}{H'}\right)\dot{\boldsymbol{s}} = 2G_{\max}\dot{\boldsymbol{e}}, \tag{2}$$

given in terms of their rates, $\dot{\boldsymbol{s}}$ and $\dot{\boldsymbol{e}}$, respectively. Here, $G_{\max}$ represents the maximum shear modulus.

The fact that the material is purely deviatoric implies that $\dot{\boldsymbol{s}}$ and $\dot{\boldsymbol{e}}$ are in the same direction. That being the case, the integral of Equation 2 can be expressed as a nonlinear scalar equation of the form

$$\psi + 3G_{\max}\psi\left(\frac{1-\beta}{H'_n} + \frac{\beta}{H'_{n+1}}\right) = 2G_{\max}, \tag{3}$$

where H'_n and H'_{n+1} are the hardening values corresponding to the n (known) and $n+1$ (unknown) states, β is the integration parameter, and ψ is an unknown positive scalar representing an equivalent shear modulus. This latter parameter is such that it satisfies a proportionality between the changes (Δ) in stress and strain as

$$\Delta \boldsymbol{s} = \psi \Delta \boldsymbol{e}. \tag{4}$$

In turn, in the context of bounding surface plasticity, the hardening function depends on the positive scalar κ, which satisfies the interpolation function

$$\| \boldsymbol{s} + \kappa \left(\boldsymbol{s} - \boldsymbol{s}_0 \right) \| = R, \tag{5}$$

where $\boldsymbol{s}_0$ is the last unloading deviatoric stress tensor and R is the maximum material capacity, which is defined in terms of the undrained shear strength S_u as

$$R = S_u \sqrt{8/3}. \tag{6}$$

Using Equation 4, the discrete version of (5) can be written in terms of the known deviatoric stress at n and its change with deviatoric strain as

$$\| \boldsymbol{s}_n + \psi \Delta \boldsymbol{e} + \kappa_{n+1} \left(\boldsymbol{s}_n + \psi \Delta \boldsymbol{e} - \boldsymbol{s}_0 \right) \| = R. \tag{7}$$

Both Equations 3 and 7 are nonlinear in two variables, ψ and κ_{n+1}. They can therefore be solved simultaneously to provide for the material update of the total stress $\boldsymbol{\sigma}_{n+1}$ in terms of previous stress $\boldsymbol{\sigma}_n$ and the increments of total ($\boldsymbol{\varepsilon}$) and deviatoric ($\boldsymbol{e}$) strains as

$$\boldsymbol{\sigma}_{n+1} = \boldsymbol{\sigma}_n + K \mathrm{Tr}(\Delta \boldsymbol{\varepsilon}) \mathbf{1} + \psi \Delta \boldsymbol{e}, \tag{8}$$

where K is the elastic bulk modulus, Tr is the trace operator, and $\mathbf{1}$ is the second order unit tensor.

In the work presented here, the numerical integration of these equations is done explicitly with substepping and an automatic error control method (see Sloan et al[28] and Andrianopoulos et al[29]).

3 | HARDENING FUNCTION

It follows from the previous section that the hardening function H' is essential to the material update. This section reviews the general formulation of H' in terms of an arbitrary 1D backbone function f following standard concepts of 1D plasticity.

Let the stress-strain relationship of the material be described by a function f such as that one represented by the thick line along the initial loading path ① in Figure 1. This function can be written as

$$\bar{\tau} = f\left(\bar{\gamma}\right), \tag{9}$$

where $\bar{\tau} = \tau / \tau_{\mathrm{ref}}$ and $\bar{\gamma} = \gamma / \gamma_{\mathrm{ref}}$ are the relative stress and strain, measured with respect to a reference state satisfying the condition $\tau_{\mathrm{ref}} = G_{\max} \gamma_{\mathrm{ref}}$.

It follows from this that the tangent modulus E_t of the backbone function can be directly obtained by differentiating f with respect to $\bar{\gamma}$ to obtain

$$E_t = 2 G_{\max} \frac{df}{d\bar{\gamma}}. \tag{10}$$

Then, according to standard concepts from the theory of elastoplasticity, the hardening function H' can be defined as

$$H' = \frac{2}{3} K_p, \tag{11}$$

where K_p is the 1D plastic modulus given by

$$K_p = \frac{2 E_t}{2 - E_t / G_{\max}}. \tag{12}$$

Using Equation 10 in Equation 12, and subsequently replacing K_p in Equation 11, the hardening function can be written in terms of the relative strain as

$$\frac{H'(\bar{\gamma})}{3 G_{\max}} = \frac{df / d\bar{\gamma}}{1 - df / d\bar{\gamma}}. \tag{13}$$

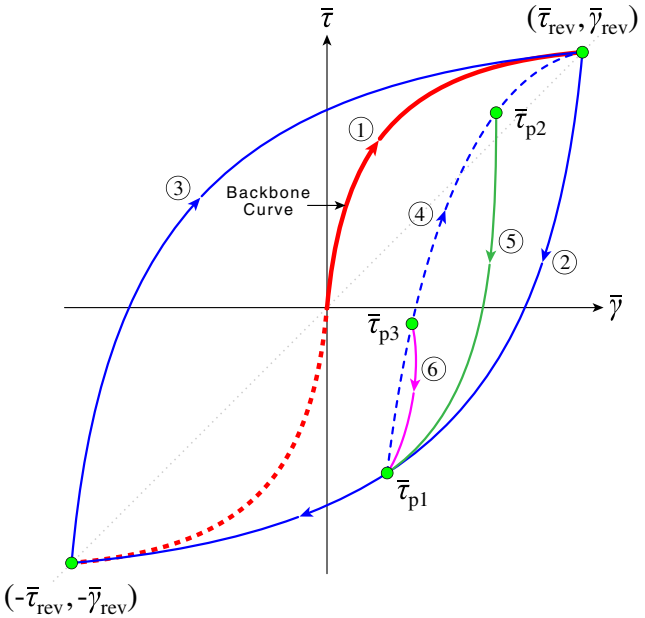

FIGURE 1 Schematic description of hysteresis cycles representing the stress-strain relationship in terms of the relative stress $\bar{\tau}$ and the relative strain $\bar{\gamma}$. The thick continuous line represents the initial loading path or backbone curve as indicated. Subsequent loading and unloading paths follow the second extended Masing rule, with their orientations indicated by arrows along the lines. Circled numbers are used for select paths for reference [Colour figure can be viewed at wileyonlinelibrary.com]

In the bounding surface framework, H' must be specified in terms of κ, with κ being such that the extreme conditions where the material transitions from perfect elasticity at unloading (ie, $\kappa = \infty$) to perfect plasticity at the bounding surface (ie, $\kappa = 0$) are fulfilled from the scalar form of Equation 5, in which case $\boldsymbol{s}$ and R become τ and τ_{ref}, respectively, leading to

$$\bar{\tau} = \frac{1}{(1+\kappa)}. \tag{14}$$

Note that Equation 14 provides a $\bar{\tau} - \kappa$ relationship for the backbone curve, and that $\tau_{max} = \tau_{ref}$ is assumed. Then, substituting Equation 14 in Equation 9, the latter becomes

$$\frac{1}{(1+\kappa)} = f(\bar{\gamma}). \tag{15}$$

This means that for any given κ, H' can be determined by solving Equation 15 for $\bar{\gamma}$ and using the result in Equation 13.

4 | PROPOSED FORMULATION

Obviating some of the details, the method put forward by Borja and Amies[15] is based on the combination of Equations 8 and 13 and the other companion expressions described in the previous two sections. This approach has proven to be very useful in geotechnical modeling. However, as pointed out by Montáns,[20] the cycles in this formulation do not recover the initial loading curve, nor do they become stable upon the first cycle or comply with Masing rules, causing loading and unloading curves to change with the stress level. The proposed formulation described ahead provides a solution to these problems while preserving the simplicity inherited from Borja and Amies[15] and avoiding the additional complexities introduced by other alternative solutions (eg, previous studies[20-24]). This is done by introducing new functions for unloading branches and partial cycles, while also allowing the use of damping reduction factors.

4.1 | Masing rules and damping reduction

Traditional 1D models rely on extended Masing rules to define the course of loading and unloading paths in hysteresis loops. In particular, using Figure 1 as reference, the second extended Masing rule establishes that if reverse loading occurs

at $(\bar{\tau}_{\text{rev}}, \bar{\gamma}_{\text{rev}})$, the unloading path ② is controlled by

$$\frac{\bar{\tau}_{\text{rev}} - \bar{\tau}}{2} = f\left(\frac{\bar{\gamma}_{\text{rev}} - \bar{\gamma}}{2}\right), \tag{16}$$

which is nothing but a doubled-and-reversed version of the backbone loading path ①.

It is broadly recognized that this approach results in hysteresis loops that overestimate damping (ξ). To limit this effect, a modulus reduction and damping-curve fitting procedure was proposed by Phillips and Hashash[27] on the basis of the damping reduction factor F_{γ_m} introduced by Darendeli.[26] Although the formulation proposed by Phillips and Hashash[27] is restricted to hyperbolic backbone functions, it can be adapted for more general loading/unloading criteria through a simple manipulation, leading to a modified version of Equation 16 expressed as

$$\frac{\bar{\tau}_{\text{rev}} - \bar{\tau}}{2} = F_{\gamma_m} f\left(\frac{\bar{\gamma}_{\text{rev}} - \bar{\gamma}}{2}\right) + \left(1 - F_{\gamma_m}\right) \bar{G}_{\gamma_m}\left(\frac{\bar{\gamma}_{\text{rev}} - \bar{\gamma}}{2}\right). \tag{17}$$

Here, $\bar{G}_{\gamma_m} = G_{\gamma_m}/G_{\max}$, where G_{γ_m} is the secant shear modulus at the maximum shear strain γ_m. It should be noted that Equation 17 is equivalent to the generalized formulation recently presented by Numanoglu et al[25] in an otherwise simultaneous and uncoordinated effort to the one presented here.

There are two alternative expressions for F_{γ_m}. These are respectively given by Darendeli[26] and Phillips and Hashash[27] as

$$F_{\gamma_m} = p_1\left(\bar{G}_{\gamma_m}\right)^{p_2} \tag{18a}$$

and

$$F_{\gamma_m} = p_1 - p_2\left(1 - \bar{G}_{\gamma_m}\right)^{p_3}, \tag{18b}$$

where p_1, p_2, and p_3 are parameters that are calibrated to fit a given γ-ξ curve.

Introducing

$$\bar{\tau}_d = \frac{\bar{\tau}_{\text{rev}} - \bar{\tau}}{2},$$
$$\bar{\gamma}_d = \frac{\bar{\gamma}_{\text{rev}} - \bar{\gamma}}{2},$$

and

$$\eta_{\gamma_m} = \left(1 - F_{\gamma_m}\right) \bar{G}_{\gamma_m},$$

Equation 17 can be reduced to

$$\bar{\tau}_d = F_{\gamma_m} f\left(\bar{\gamma}_d\right) + \eta_{\gamma_m} \bar{\gamma}_d. \tag{19}$$

It follows from this that $\bar{\gamma}_d$ is equivalent to $\bar{\gamma}$. Therefore, a similar approach to that used before for Equation 13 can be used here to write a hardening function for the unloading/reloading paths as

$$\frac{H'(\bar{\gamma})}{3G_{\max}} = \frac{F_{\gamma_m} df/d\bar{\gamma} + \eta_{\gamma_m}}{1 - F_{\gamma_m} df/d\bar{\gamma} - \eta_{\gamma_m}}. \tag{20}$$

Notice that when $F(\gamma_m) = 1$, Equation 20 is the same as Equation 13.

On the other hand, in the κ-space, the unloading stress path is such that it satisfies

$$\kappa = \frac{\tau_{\text{ref}} + \tau}{\tau_{\text{rev}} - \tau}, \tag{21}$$

which can be written as

$$\bar{\tau} = \frac{\kappa \bar{\tau}_{\text{rev}} - 1}{1 + \kappa}. \tag{22}$$

Here, $\bar{\tau}_{\text{rev}} = \tau_{\text{rev}}/\tau_{\text{ref}}$. Replacing Equation 22 in Equation 19, the latter becomes

$$\frac{\varphi_{\text{rev}}}{(1 + \kappa)} = F_{\gamma_m} f\left(\bar{\gamma}\right) + \eta_{\gamma_m} \bar{\gamma}, \tag{23}$$

where $\varphi_{\text{rev}} = (1 + \bar{\tau}_{\text{rev}})/2$. It is important to point out that Equation 15 can be recovered from Equation 23 if both $F_{\gamma_m} = 1$ and $\varphi_{\text{rev}} = 1$ (ie, no damping reduction applied, and $\tau_{\text{rev}} = \tau_{\text{ref}}$).

Equations 20 and 23 define the hardening function of the unloading branch in accordance with the second Masing rule. Moreover, since the reloading path ③ is the mirrored version of the unloading path ② with respect to the axis that runs through the points $(-\bar{\tau}_{\text{rev}}, -\bar{\gamma}_{\text{rev}})$ and $(\bar{\tau}_{\text{rev}}, \bar{\gamma}_{\text{rev}})$ in Figure 1, these equations also represent the hardening reloading function.

Attention is now drawn to the third Masing rule. This rule establishes that after the unloading curve intersects the backbone function, the stress-strain relationship must follow the backbone curve until the next reload/unload occurs. The intersection stress with the backbone curve occurs at $\bar{\tau} = -\bar{\tau}_{\text{rev}}$, which if replaced in Equation 21 provides the transition point

$$\kappa_o = \frac{\tau_{\text{ref}} - \tau_{\text{rev}}}{2\tau_{\text{rev}}} = \frac{1}{2}\left(\frac{1}{\bar{\tau}_{\text{rev}}} - 1\right) \tag{24}$$

between the unloading and skeleton curves.

Now, to use the hardening functions in the multiaxial space, one needs to define the reversal stress $\bar{\tau}_{\text{rev}}$. Therefore, in the general stress state, it is proposed here to make τ_{rev} equal to the norm of the deviatoric component of the reversal stress tensor $||\boldsymbol{s}_{\text{rev}}|| = \sqrt{\boldsymbol{s}_{\text{rev}} : \boldsymbol{s}_{\text{rev}}}$ and to normalize this tensor with respect to the radius of the bounding surface R. This means that

$$\bar{\tau}_{\text{rev}} = \frac{\tau_{\text{rev}}}{\tau_{\text{ref}}} \equiv \frac{||\boldsymbol{s}_{\text{rev}}||}{R}, \tag{25}$$

which implies that Equation 24 becomes

$$\kappa_o = \frac{R - ||\boldsymbol{s}_{\text{rev}}||}{2||\boldsymbol{s}_{\text{rev}}||}. \tag{26}$$

In summary, given κ and τ_{rev}, Equation 20 provides a general function for the backbone and unloading-reloading curves in accordance with the second and third Masing rules in terms of a normalized strain $\bar{\gamma}$ satisfying Equation 23 such that

$$\begin{aligned} \phi_{\text{rev}} &= 1, \text{ and} \\ F_{\gamma_m} &= 1 \end{aligned} \tag{27a}$$

if $\kappa \leq \kappa_o$, or

$$\begin{aligned} \phi_{\text{rev}} &= (R + ||\boldsymbol{s}_{\text{rev}}||)/2R, \text{ and} \\ F_{\gamma_m} &\quad \text{from Equation 18} \end{aligned} \tag{27b}$$

otherwise.

4.2 | Partial cycles

A complete formulation should also provide for partial cycles that originate at secondary stress reversals within the major branches of the hysteresis loops. Since inner loops must satisfy the fourth extended Masing rule, then some minor modifications to φ_{rev} and κ_o must be done to reflect the fact that partial cycles span across fixed stress intervals of magnitude lower than τ_{rev}.

Consider, for instance, the inner reloading path ④ in Figure 1 in the one-dimensional formulation. Here, the current stress $\tau_c = \tau_{\text{p1}}$ and the former stress $\tau_f = \tau_{\text{rev}}$ are such that $\tau_{\text{c}}\tau_{\text{f}} < 0$. In the general stress state case, this condition is equivalent to

$$\kappa_c \leq \frac{R}{||\boldsymbol{s}_{\text{f}}||}, \tag{28}$$

where the bounding surface parameter of the current stress reversal κ_c is defined as

$$\kappa_c = \frac{R - ||\boldsymbol{s}_{\text{f}}||}{||\boldsymbol{s}_{\text{f}}|| + ||\boldsymbol{s}_{\text{c}}||} \tag{29}$$

and $\boldsymbol{s}_{\text{c}}$ and $\boldsymbol{s}_{\text{f}}$ are the current and former reverse stress tensors, respectively (ie, the start point and end point of the inner branch ④).

If another stress reversal occurs during reloading (see τ_{p2} and path ⑤ in Figure 1), then $\boldsymbol{s}_{\text{f}}$ and $\boldsymbol{s}_{\text{c}}$ need to be reset to the particular values of the nested branch, and Equations 28 and 29 are recomputed accordingly.

Therefore, once Equation 28 is satisfied, the lower limit of κ associated with the inner branch becomes $\kappa_o = \kappa_{o\text{I}}$, where

$$\kappa_{o\text{I}} = \frac{R - ||\boldsymbol{s}_{\text{f}}||}{||\boldsymbol{s}_{\text{f}}|| + ||\boldsymbol{s}_{\text{c}}||}. \tag{30}$$

On the other hand, unloading branches such as stress path ⑥ in Figure 1 are represented by the inequality

$$\kappa_c > \frac{R}{\|\boldsymbol{s}_\mathrm{f}\|}. \tag{31}$$

In this case, the current and former stresses, respectively given by $\tau_\mathrm{c} = \tau_{\mathrm{p}2}$ and $\tau_\mathrm{f} = \tau_{\mathrm{p}1}$, satisfy $\tau_\mathrm{c}\tau_\mathrm{f} > 0$. Subsequently, the lower limit of κ becomes $\kappa_o = |\kappa_{o\mathrm{II}}|$, where

$$\kappa_{o\mathrm{II}} = \frac{R - \|\boldsymbol{s}_\mathrm{f}\|}{\|\boldsymbol{s}_\mathrm{f}\| - \|\boldsymbol{s}_\mathrm{c}\|}. \tag{32}$$

In either case, one should use $\|\boldsymbol{s}_\mathrm{rev}\| = \|\boldsymbol{s}_\mathrm{c}\|$ in Equation 27b.

5 | FORMULATION EVALUATION

The following two sections present an evaluation of the proposed formulation. In particular, Equation 20 and the other expressions put forward to satisfy the Masing rules during complete and partial loading and unloading cycles are tested for three well-known hyperbolic models, namely, the KZ,[2] the MKZ[3], and the GQ/H[4] models. These models are chosen because they formulate the hardening function in a continuous analytical form, which facilitates obtaining closed-form solutions for numerical verification—at least for the no damping reduction case. It should be noted that this choice is one of convenience given that there is no limitation to using the proposed formulation for models formulated in piecewise or discrete forms.

5.1 | The KZ model

Konder and Zelasko[2] define the normalized backbone stress-strain relationship with the hyperbolic function

$$\bar{\tau} = f_{\mathrm{KZ}}(\bar{\gamma}) = \frac{\bar{\gamma}}{1+\bar{\gamma}}. \tag{33}$$

Substituting Equation 33 in Equations 20 and 23 yields

$$\frac{H'_{\mathrm{KZ}}}{3G_{\max}} = \frac{F_{\gamma_m}/(1+\bar{\gamma})^2 + \eta_{\gamma_m}}{1 - F_{\gamma_m}/(1+\bar{\gamma})^2 - \eta_{\gamma_m}} \tag{34}$$

and

$$\frac{\varphi_{\mathrm{rev}}}{(1+\kappa)} = F_{\gamma_m}\frac{\bar{\gamma}}{1+\bar{\gamma}} + \eta_{\gamma_m}\bar{\gamma}. \tag{35}$$

Equation 35 is quadratic in $\bar{\gamma}$. Therefore, in the most general case

$$\bar{\gamma} = \frac{1}{2a}\left(-b + \sqrt{b^2 - 4ac}\right), \tag{36a}$$

with

$$\begin{aligned} a &= \eta_{\gamma_m}, \\ b &= F_{\gamma_m} + \eta_{\gamma_m} - \varphi_{\mathrm{rev}}/(1+\kappa), \text{ and} \\ c &= -\varphi_{\mathrm{rev}}/(1+\kappa). \end{aligned} \tag{36b}$$

Then, upon solving $\bar{\gamma}$ using Equation 36 for any given κ and $\bar{\tau}_{\mathrm{rev}}$ condition, one can solve Equation 34.

To illustrate this, the simpler case of no damping reduction is considered here, where $F_{\gamma_m} = 1$, $\eta_{\gamma_m} = 0$, and the normalized strain becomes

$$\gamma_m = \frac{\varphi_{\mathrm{rev}}}{1 + \kappa - \varphi_{\mathrm{rev}}}. \tag{37}$$

Substituting Equation 37 in Equation 34 leads to

$$\frac{H'(\kappa)}{3G_{\max}} = \frac{(1+\kappa-\varphi_{\mathrm{rev}})^2}{\varphi_{\mathrm{rev}}\,(2+2\kappa-\varphi_{\mathrm{rev}})}. \tag{38}$$

Recall that for $\varphi_{\mathrm{rev}} = 1$, the general hardening function is the hardening function of the backbone curve. In that case, Equation 38 becomes

$$\frac{H'(\kappa)}{3G_{\max}} = \frac{\kappa^2}{1+2\kappa}, \tag{39}$$

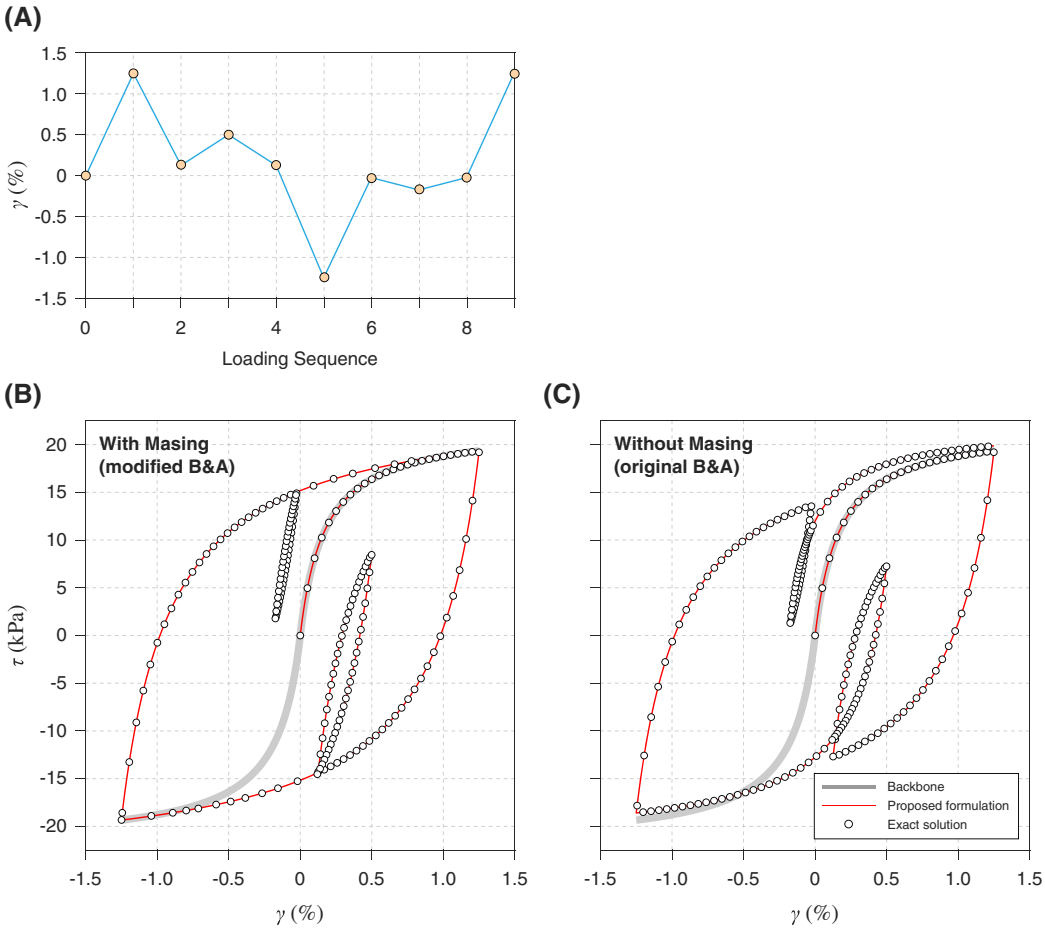

FIGURE 2 Stress-strain evolution as an implicit function of time for a cyclic shear loading sequence using the Konder-Zelasko model. The thick line represents the backbone function, the dots represent the exact solution from the hyperbolic function, and the thin line represents the results of the multiaxial material integration. A, Loading sequence in terms of imposed shear strain. B, Results including the proposed extended Masing rules. C, Results obtained using the backbone hardening function without considering Masing rules [Colour figure can be viewed at wileyonlinelibrary.com]

which is identical to the hardening function of the hyperbolic model presented in equation 24 of Borja and Amies.[15] Replacing $\varphi_{\text{rev}} = (1 + \bar{\tau}_{\text{rev}})/2$ in Equations 38 and 39 and combining these two equations result in

$$\frac{H'(\kappa, \bar{\tau}_{\text{rev}})}{3G_{\max}} = \begin{cases} \dfrac{\kappa^2}{(1+2\kappa)} & \text{if } \kappa \le \kappa_o \\ \dfrac{(2\kappa + 1 - \bar{\tau}_{\text{rev}})^2}{(1+\bar{\tau}_{\text{rev}})(4\kappa + 3 - \bar{\tau}_{\text{rev}})} & \text{otherwise} \end{cases} \tag{40a}$$

with

$$\kappa_o = \frac{R - \tau_{\text{rev}}}{2\tau_{\text{rev}}} = \frac{1}{2}\left(\frac{1}{\bar{\tau}_{\text{rev}}} - 1\right), \tag{40b}$$

where when in the general stress state, $\tau_{\text{rev}} = ||\boldsymbol{s}_{\text{rev}}||$ and $\bar{\tau}_{\text{rev}} = ||\boldsymbol{s}_{\text{rev}}||/R$.

As an example, consider a material characterized by the KZ stress-strain relationship with $G_{\max} = 12\,800$ kPa and $\tau_{\text{ref}} = 22$ kPa under an applied loading cycle consisting of the imposed simple shear strain sequence $\gamma(\%) = \{1.25, 0.125, 0.5, -1.25, -0.025, -0.175, 1.5\}$ shown in Figure 2A. Then, Figure 2B and 2C illustrates the outcome of the numerical and exact solutions for the original and modified formulations proposed in this study. Here, for the case without Masing, Figure 2C is nothing else but a direct comparison between the proposed numerical formulation and the original work of Borja and Amies.[15] Likewise, in similar subsequent figures for the MKZ and GQ/H models, the comparisons for the cases without Masing will correspond to implementations of the original mathematical framework of Borja and Amies.[15]

For the particular example shown in Figure 2, no damping reduction is assumed. It should be noted that in the multiaxial space, the strain regime is addressed by making zero all the components of the total stress tensor except $\varepsilon_{23} = \varepsilon_{32} = \gamma/2$. As it can be seen from this figure, in both cases, with and without adopting Masing rules, the numerical results perfectly match the exact solutions.

5.2 | The MKZ model

The MKZ model emerged as an improvement to the KZ model to better represent the behavior of soils at moderate strain levels. Matasovic[3] defines the normalized backbone function of this model as

$$\bar{\tau} = f_{\text{MKZ}}(\bar{\gamma}) = \frac{\bar{\gamma}}{1 + \beta \bar{\gamma}^s}, \tag{41}$$

where β and s are material parameters calibrated to fit a target $G/G_{\max}$ curve and $\bar{\tau} = \tau/\tau_{\text{ref}}$, where τ_{ref} is arbitrarily set as the upper shear stress resistance in the 1% to 3% strain range. Then, following similar steps to those in the previous section, one obtains the H' and $\bar{\gamma}$ expressions for the MKZ model as

$$\frac{H'_{\text{MKZ}}}{3G_{\max}} = \frac{\eta_{\gamma_m}(1 + \beta\bar{\gamma}^s)^2 + F_{\gamma_m}\left[1 + (1-s)\beta\bar{\gamma}^s\right]}{\left(1 - \eta_{\gamma_m}\right)(1 + \beta\bar{\gamma}^s)^2 - F_{\gamma_m}\left[1 + (1-s)\,\beta\bar{\gamma}^s\right]} \tag{42a}$$

and

$$\frac{\varphi_{\text{rev}}}{1 + \kappa} = \frac{F_{\gamma_m}\bar{\gamma}}{1 + \beta\bar{\gamma}^s} + \eta_{\gamma_m}\bar{\gamma}\,. \tag{42b}$$

Unlike in the case of the KZ model, here it is necessary to solve $\bar{\gamma}$ in Equation 42b numerically before replacing it in Equation 42a. To that end, in this study, the Pegasus method proposed by King[30] is preferred over conventional Newton-Raphson techniques to avoid computing Jacobian terms.

As an example, consider the case of no damping reduction (ie, $F_{\gamma_m} = 1$ and $\eta_{\gamma_m} = 0$), where Equation 42a becomes

$$\frac{H'_{\text{MKZ}}}{3G_{\max}} = \frac{1 + (1-s)\beta\bar{\gamma}^s}{\beta\bar{\gamma}^s\,(1 + s + \beta\bar{\gamma}^s)}, \tag{43}$$

and a clayey material of properties—$\tau_{\text{ref}} = 15$ kPa, $G_{\max} = 12800$ kPa, Poisson ratio $\nu = 0.49$, effective vertical stress $\sigma'_0 = 100$ kPa, overconsolidation ratio OCR $= 4$, coefficient of lateral earth pressure $K_0 = 0.65$, and plastic index PI $= 20$, under $N = 10$ number of loading cycles, at a loading frequency $f = 5$ Hz—for which $\beta = 1.545$ and $s = 0.915$ are calibrated using the software Deepsoil[31] to fit the $G/G_{\max}$ curve proposed by Darendeli[26] for clays.

Then consider this soil specimen subjected to the same strain regime used in the previous section for the KZ model. Under these conditions, one obtains the results presented in Figure 3. As in the case of the KZ model, the results shown in Figure 3 for the MKZ model render an excellent agreement between the numerical and exact solutions. Of particular interest is the fact that in this case, for these conditions and model, the results suggest a larger deviation from the reloading stress with respect to the backbone curve than in the previous KZ model.

It should be noted that in the π-plane, this (and the previous) numerical experiment fall in the category of radial loading, with a Lode angle $\theta = 0°$. As a result, the multiaxial response naturally reduces itself to a scalar equation, which is what facilitates the direct comparison with the backbone function.

Another instance where radial loading emerges is that of undrained cyclic triaxial tests, ie, when $\theta = 90°$. This condition is tested for the same overconsolidated clay material just used. In this case, the specimen is subjected to a loading/reloading cycle at a maximum axial strain of $\varepsilon_{11} = \pm 0.5\%$. To ensure a truly undrained response, the radial strains are set to $\varepsilon_{22} = \varepsilon_{33} = -\varepsilon_{11}/2$. Unlike the previous two experiments, this case considers damping reduction. In particular, Equation 24 is used adopting F_{γ_m} as given by Equation 18b with parameters $p_1 = 0.654$, $p_2 = 0.248$, and $p_3 = 3.25$. In addition, to compute $\bar{G}_{\gamma_m}$, a generalization in terms of the maximum deviatoric total strain and stress tensors where $\bar{G}_{\gamma_m} = ||\boldsymbol{s}_m||/||\boldsymbol{e}_m||/(2G_{\max})$ was adopted. This approach renders $\bar{G}_{\gamma_m} = 0.0941$.

The results of this third numerical experiment are shown in Figure 4. This figure shows the normal stress-strain hysteresis loops for the cases with and without damping reduction and compares the numerical and exact solutions in terms of the deviatoric stress ratio $q/\sqrt{3}\tau_{\max}$ with respect to the normal strain ε_{11}, where $q = \sqrt{3J_2}$. As in the previous two experiments, here, the numerical and exact solutions match perfectly. In addition, the effect of the damping reduction factor is evident from the normal stress stress-strain loops, which become thinner than the case with no damping reduction.

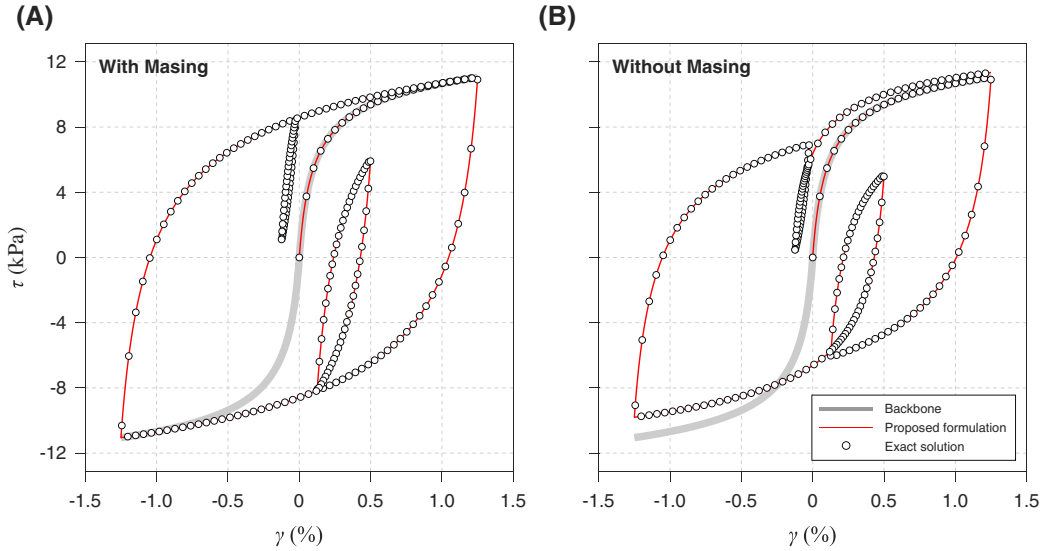

FIGURE 3 Stress-strain evolution as an implicit function of time using the modified Konder-Zelasko model for the same loading sequence shown in Figure 2A. The thick line represents the backbone function, the dots represent the exact solution from the hyperbolic function, and the thin line represents the results of the multiaxial material integration. A, Results including the proposed extended Masing rules. B, Results obtained using the backbone hardening function without considering Masing rules [Colour figure can be viewed at wileyonlinelibrary.com]

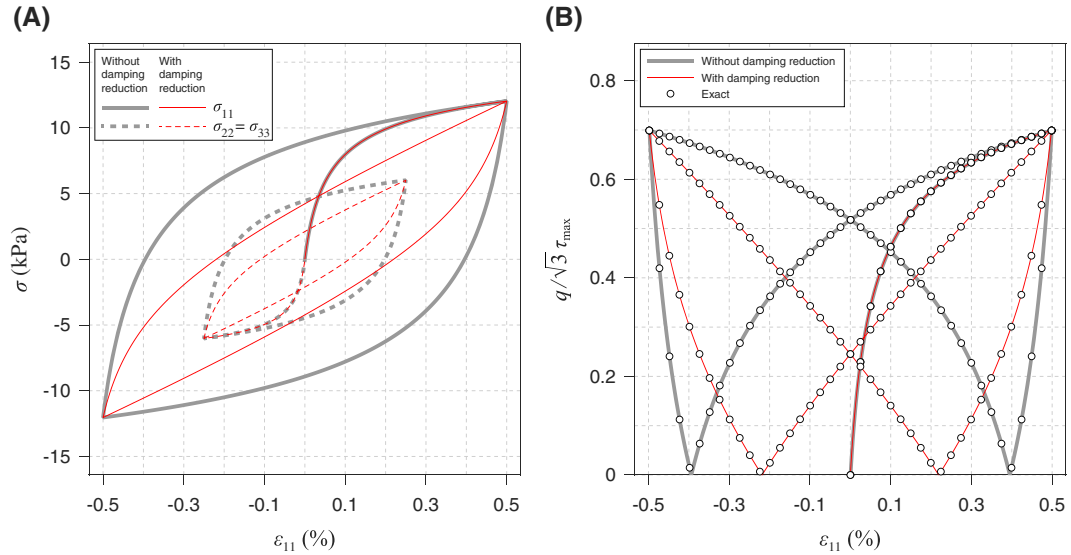

FIGURE 4 Cyclic triaxial test considering the formulation proposed for Masing rules, with and without damping reduction for the modified Konder-Zelasko model. A, Hysteresis loops of the normal stresses-strain relationship as an implicit function of time. B, Evolution of the deviatoric stress ratio $q/\sqrt{3}\tau_{\max}$ with respect to normal strain, also as an implicit function of time, compared with respect to the exact solution [Colour figure can be viewed at wileyonlinelibrary.com]

5.3 | The GQ/H model

Finally, this section considers the case of the GQ/H model introduced by Groholski et al.[4] In this case, the backbone function is defined as

$$\bar{\tau} = f_{\text{GQH}} = \frac{2\bar{\gamma}}{1 + \bar{\gamma} + \sqrt{(1+\bar{\gamma})^2 - 4\theta_\tau \bar{\gamma}}} \tag{44}$$

and τ_{ref} in $\bar{\tau} = \tau/\tau_{\text{ref}}$ is taken equal to $\tau_{\max}$. Here, the parameter θ_τ is given by

$$\theta_\tau = \theta_1 + \theta_2 \frac{\theta_4 \bar{\gamma}^{\theta_5}}{\theta_3^{\theta_5} + \theta_4 \bar{\gamma}^{\theta_5}} \leq 1.0, \tag{45}$$

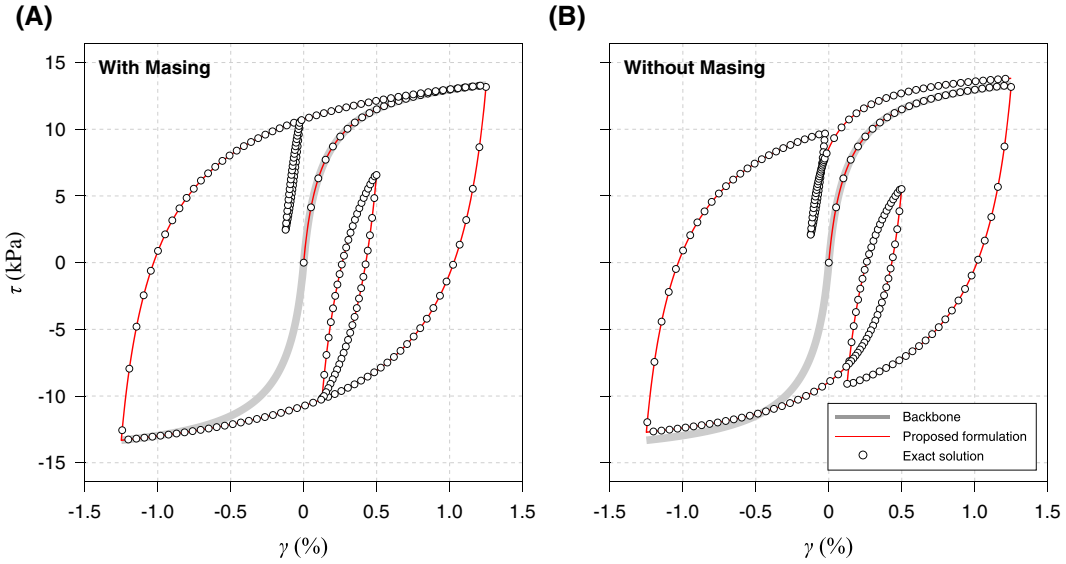

FIGURE 5 Stress-strain evolution as an implicit function of time using the GQ/H model for the same loading sequence shown in Figure 2A. The thick line represents the backbone function, the dots represent the exact solution from the hyperbolic function, and the thin line represents the results of the multiaxial material integration. A, Results including the proposed extended Masing rules. B, Results obtained using the backbone hardening function without considering Masing rules [Colour figure can be viewed at wileyonlinelibrary.com]

where the coefficients θ_i for $i = 1, \ldots, 5$ are calibrated to fit a given degradation curve $G/G_{\max}$.

Replacing Equation 44 in Equations 20 and 23, one obtains

$$\frac{H'_{\mathrm{GQ/H}}}{3G_{\max}} = \frac{2F_{\gamma_m}\left(\Gamma_1 - \bar{\gamma}\Gamma_2\right) + \eta_{\gamma_m}\Gamma_1^2}{\left(1 - \eta_{\gamma_m}\right)\Gamma_1^2 - 2F_{\gamma_m}\left(\Gamma_1 - \bar{\gamma}\Gamma_2\right)} \tag{46a}$$

and

$$\frac{\varphi_{\mathrm{rev}}}{1+\kappa} = \frac{2F_{\gamma_m}\bar{\gamma}}{\Gamma_1} + \eta_{\gamma_m}\bar{\gamma}, \tag{46b}$$

where

$$\Gamma_1 = 1 + \bar{\gamma} + \sqrt{(1+\bar{\gamma})^2 - 4\theta_\tau\bar{\gamma}}, \tag{47a}$$

$$\Gamma_2 = 1 + \frac{\left(1 + \bar{\gamma} - 2\left(\theta_\tau + \bar{\gamma}\Gamma_3\right)\right)}{\sqrt{(1+\bar{\gamma})^2 - 4\theta_\tau\bar{\gamma}}}, \tag{47b}$$

and

$$\Gamma_3 = \frac{\theta_2\theta_3^{\theta_5}\theta_4\theta_5\bar{\gamma}^{\theta_5-1}}{\left(\theta_3^{\theta_5} + \theta_4\bar{\gamma}^{\theta_5}\right)^2}. \tag{47c}$$

In this case, the hardening function for no damping reduction becomes

$$\frac{H'_{\mathrm{GQ/H}}}{3G_{\max}} = \frac{2\left(\Gamma_1 - \bar{\gamma}\Gamma_2\right)}{\Gamma_1^2 - 2\left(\Gamma_1 - \bar{\gamma}\Gamma_2\right)}. \tag{48}$$

Equations 48 and 46a are used to solve the same two problems considered for the MKZ model. Here, the curve fitting parameters were also obtained using Deepsoil (see Hashash et al[31]), which delivered the values $\theta_1 = -1.02$, $\theta_2 = 0.63$, $\theta_3 = 0.0145$, $\theta_4 = 1$, and $\theta_5 = 0.80$. The results are shown in Figures 5 and 6 for the pure shear and undrained cyclic triaxial tests, respectively. In the case of the triaxial test, $\bar{G}_{\gamma_m} = 0.115$. Here, as well as in all previous cases, the match between the numerical and exact solutions provides confidence on the proposed formulation.

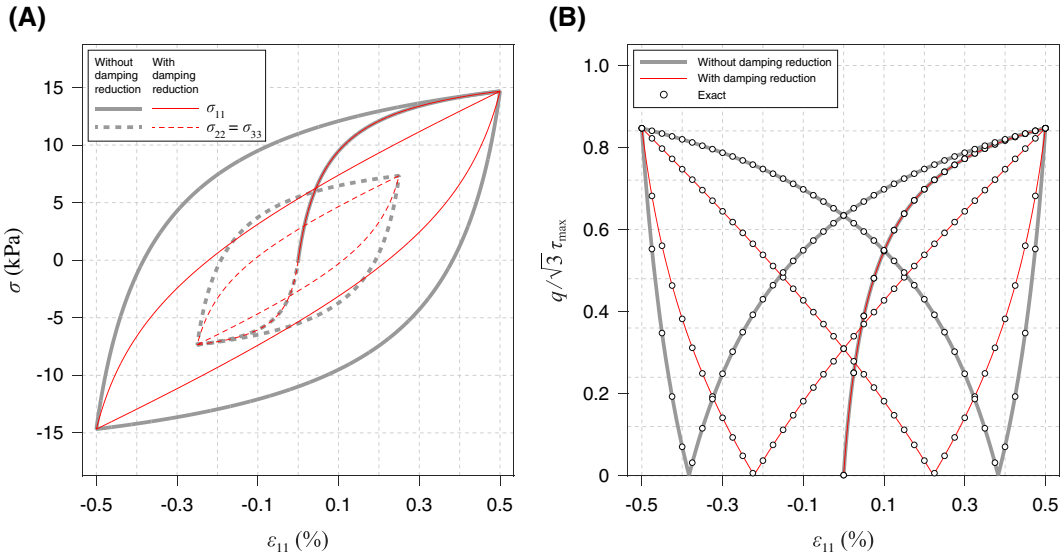

FIGURE 6 Cyclic triaxial test considering the formulation proposed for Masing rules, with and without damping reduction for the GQ/H model. A, Hysteresis loops of the normal stresses-strain relationship as an implicit function of time. B, Evolution of the deviatoric stress ratio $q/\sqrt{3}\tau_{max}$ with respect to normal strain, also as an implicit function of time, compared with respect to the exact solution [Colour figure can be viewed at wileyonlinelibrary.com]

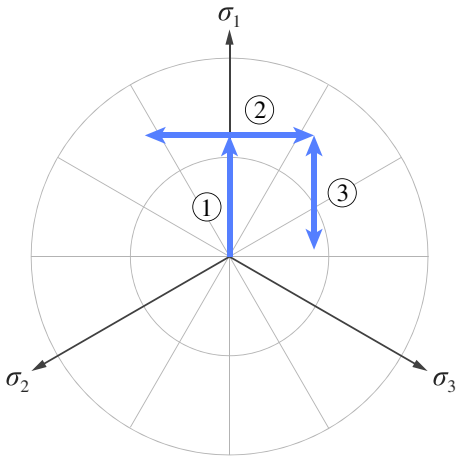

FIGURE 7 Schematic representation of the loading sequence on the π-plane as used on a clay specimen with the proposed formulation applied to the GQ/H model corresponding to the multiaxial response shown in Figure 8 [Colour figure can be viewed at wileyonlinelibrary.com]

Finally, to present a more complete picture of the performance of the proposed formulation, the same clayey material is subjected to a loading combination of cyclic triaxial, simple cyclic shear, and cyclic triaxial, as depicted by the loading paths ①, ②, and ③ in Figure 7. The response, computed using the hardening function associated with the GQ/H model without damping reduction, is shown in Figure 8. In this case, the initial triaxial stage incorporates a small unloading/reloading cycle as highlighted by a zoom-in lens in Figure 8. This triggers an overshooting effect and leads the non-Masing response (dashed line) to reach a normal stress ratio near 1, whereas the formulation complying with the Masing rule returns to the initial loading path (continuous line) reaching a maximum stress ratio of about 0.8.

Moving on, in the second loading stage (cyclic shear), the magnitude of the normal stress is locked. As a result, changes in the total stress tensor correspond to those defined by the evolution of the off-diagonal stresses, shown in Figure 8B. The third and final loading stage mobilizes the normal stresses once again. In general, one could argue that the discrepancy originated by the small unloading/reloading cycle put aside, the results of this experiment seem to indicate that both approaches, with and without applying Masing rules, lead to similar normal stresses at the end of the loading sequence. In more complex conditions, however, the differences may be more significant.

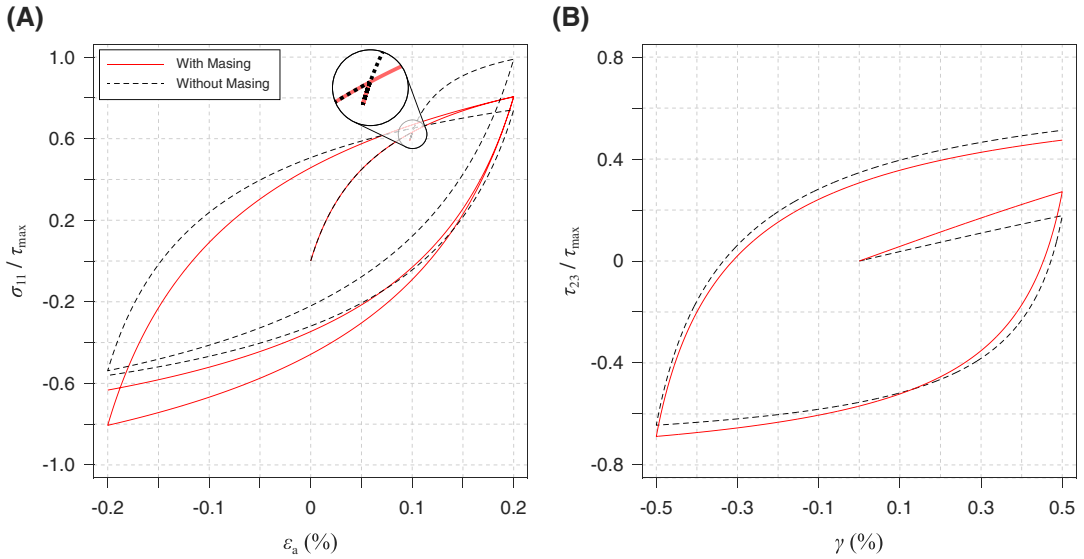

FIGURE 8 Multiaxial response of a clay specimen in accordance with the proposed formulation of the hardening function for the case of the GQ/H material model for which the loading regime is composed of a sequence of cyclic triaxial, cyclic shear, and cyclic triaxial corresponding to the loading paths ①, ②, and ③ in Figure 7. A, Evolution of axial stresses normalized with respect to τ_{max} as an implicit function of time, with a zoom-in detail at the unloading/reloading cycle in the initial loading path. B, Off-diagonal (shear) stresses also normalized with respect to τ_{max} and shown as an implicit function of time [Colour figure can be viewed at wileyonlinelibrary.com]

6 | CONCLUDING REMARKS

This work lays out a formulation of hardening functions that satisfies the extended Masing rules and incorporates known damping reduction factor expressions based on one-dimensional backbone functions. This formulation builds upon the original work of Borja and Amies[15] in the context of the theory of bounding surface plasticity. In particular, it improves the referenced work by solving previously identified issues with unloading/reloading cycles and provides a consistent framework for partial and inner cycles using an explicit substepping material-update scheme with error control. This formulation was tested for three hyperbolic models (KZ, MKZ, and GQ/H) broadly used in geotechnical engineering for site response and soil-structure interaction applications. The numerical tests performed show that the formulation yields excellent agreement with reference solutions under pure shear and triaxial conditions and exhibits a good behavior under a more complex multiaxial loading condition. Although, generally speaking, the proposed approach remains within the realm of an idealized material behavior, ie, radial loading, it is the view of the authors that the work presented here is a step in the right direction towards the use of one-dimensional nonlinear models in the context of three-dimensional ground motion analysis and simulation. To that end, additional efforts are currently underway to verify the proposed framework with respect to international benchmarks and to validate its use in realistic loading conditions such as those expected during earthquake shaking. Future work will also consider comparisons of the sensitivity of results to the use of different constitutive models.

ACKNOWLEDGEMENTS

This work was supported by Universidad EAFIT and US National Science Foundation (NSF) award "SI2-SSI: Community Software for Extreme-Scale Computing in Earthquake System Science" (ACI-1450451). The authors also wish to express their gratitude to two anonymous reviewers and to the editor, Dr Ronaldo I. Borja, for their generous review and constructive comments to the original manuscript.

ORCID

Doriam Restrepo http://orcid.org/0000-0002-7575-4590
Ricardo Taborda http://orcid.org/0000-0003-0358-370X

REFERENCES

1. Ramberg W, Osgood WR. Description of stress-strain curve by three parameters.Technical Note No. 902, Washington, D.C., U.S.A., National Advisory Committee for Aeronautics; 1943.
2. Konder RL, Zelasko JS. A hyperbolic stress-strain formulation for sand. In: Proc. 2nd Pan-American Conf. Soil Mech. and Found. Eng. Sao Paulo, Brazil: Associação Brasileira de Mecânica dos Solos; July 1963;289-324.
3. Matasovic N. Seismic response of composite horizontally-layered soil deposits. *Ph.D. Thesis*. Los Angeles: Civil and Environmental EngineeringUniversity of California; 1994.
4. Groholski DR, Hashash YMA, Kim B, Musgrove M, Harmon J, Stewart J. Simplified model for small-strain nonlinearity and strength in 1D seismic site response analysis. *J Geotech Geoenviron Eng ASCE*. 2016;142(9):04016042. https://doi:10.1061/(ASCE)GT.1943-5606.0001496
5. Masing G. Internal (residual) stresses and hardening of brass (in German). In: Proc. 2nd Intl. Conf. Applied Mech.; 1926; Zürich, Switzerland. 332-335. (in German).
6. Idriss IM, Seed HB. Seismic response of horizontal soil layers. *J Soil Mech Found Div*; 94(SM4):1003-1031.
7. Idriss IM, Seed HB. Seismic response of soil deposits. *J Soil Mech Found Div*. 1970;96(SM2):631-638. Paper 7175.
8. Xu Jifeng, Bielak Jacobo, Ghattas Omar, Wang Jianlin. Three-dimensional nonlinear seismic ground motion modeling in basins. *Phys Earth Planet Inter*. 2003;137:81-95.
9. Taborda R, Bielak J, Restrepo D. Earthquake ground-motion simulation including nonlinear soil effects under idealized conditions with application to two case studies. *Seismol Res Lett*. 2012;83(6):1047-1060.
10. Dafalias YF, Popov EP. A model of nonlinearly hardening materials for complex loading. *Acta Mech*. 1975;21(3):173-192. https://doi:10.1007/BF01181053
11. Dafalias YF, Popov EP. Plastic internal variables formalism of cyclic plasticity. *J Appl Mech ASME*. 1976;43:645-651.
12. Prévost JH. Mathematical modelling of monotonic and cyclic undrained clay behaviour. *Int J Numer Anal Methods Geomech*. 1977;1(2):195-216. https://doi:10.1002/nag.1610010206
13. Prévost JH. Plasticity theory for soil stress-strain behavior. *J Eng Mech Div ASCE*. 1978;104(5):1177-1194.
14. Kramer SL. *Geotechnical Earthquake Engineering*. Prentice Hall, Upper Saddle River, New Jersey: Springer; 1996.
15. Borja RI, Amies AP. Multiaxial cyclic plasticity model for clays. *J Geotech Eng ASCE*. 1994;120(6):1051-1070.
16. Borja RI, Chao HY, Montáns FJ, Lin C-H. Nonlinear ground response at Lotung LSST site. *J Geotech Geoenviron Eng ASCE*. 1999;125(3):187-197.
17. Borja RI, Lin C-H, Sama KM, Masada GM. Modelling non-linear ground response of non-liquefiable soils. *Earthquake Engineering and Structural Dynamics*. 2000;29(1):63-83. https://doi:10.1002/(SICI)1096-9845(200001)29:1<63::AIDEQE901>3.0.CO;2-Y
18. Zhang W, Seylabi EE, Taciroglu E. Validation of a three-dimensional constitutive model for nonlinear site response and soil-structure interaction analyses using centrifuge test data. *J Numer Anal Methods Geomech*. 2017;41(18):1828-1847. https://doi:10.1002/nag.2702
19. Pisano F, Jeremic B. Simulating stiffness degradation and damping in soils via a simple visco-elastic-plastic model. *Soil Dynam Earthquake Eng*. 2014;63:98-109.
20. Montáns F-J. Bounding surface plasticity model with extended Masing behavior. *Comput Meth Appl Mech Eng*. 2000;182(1-2):135-162.
21. Fardis MN, Alibe B, Tassoulas JL. Monotonic and cyclic constitutive law for concrete. *J Eng Mech ASCE*. 1983;109(2):516-536.
22. Voyiadjis GZ, Abu-Lebdeh TM. Plasticity model for concrete using the bounding surface concept. *Int J Plast*. 1994;10(1):1-21.
23. Dafalias YF. Bounding surface plasticity I: mathematical foundation and hypoplasticity. *J Eng Mech ASCE*. 1986;112(9):966-987.
24. Mojtaba E-K, Taiebat HA. On implementation of bounding surface plasticity models with no overshooting effect in solving boundary value problems. *Comput Geotech*. 2014;55:103-116.
25. Numanoglu OA, Musgrove M, Harmon JA, Hashash YMA. Generalized non-Masing hysteresis model for cyclic loading. *J Geotech Geoenviron Eng ASCE*. 2018;144(1):06017015.
26. Darendeli MB. Development of a new family of normalized modulus reduction and material damping curves. *Ph.D. Thesis*. Austin: Civil, Architectural, and Environmental Engineering, The University of Texas; 2001. http://hdl.handle.net/2152/10396
27. Phillips C, Hashash YMA. Damping formulation for nonlinear 1D site response analyses. *Soil Dynam Earthquake Eng*. 2009;29(7):1143-1158.
28. Sloan SW, Abbo AJ, Sheng D. Refined explicit integration of elastoplastic models with automatic error control. *Eng Computations*. 2001;18(1/2):121-194.
29. Andrianopoulos KI, Papadimitriou AG, Bouckovalas GD. Explicit integration of bounding surface model for the analysis of earthquake soil liquefaction. *Int J Numer Anal Methods Geomech*. 2010;34(15):1586-1614.
30. King RF. An improved Pegasus method for root finding. *BIT Numer Math*. 1973;13(4):423-427.
31. Hashash YMA, Musgrove MI, Harmon JA, Groholski DR, Phillips CA, Park D. Deepsoil V7.0, user manual, Urbana-Champaign, Department of Civil and Environmental Engineering, University of Illinois; 2018. http://deepsoil.cee.illinois.edu

How to cite this article: Restrepo D, Taborda R. Multiaxial cyclic plasticity in accordance with 1D hyperbolic models and Masing criteria. *Int J Numer Anal Methods Geomech*. 2018;42:2095–2108. https://doi.org/10.1002/nag.2845